Shuffling atomic layer deposition gas sequences to modulate bimetallic thin films and nanoparticle properties

Shuffling Atomic Layer Deposition Gas Sequences to Modulate Bimetallic Thin Film and Nanoparticle Properties

Matthias Filez[a,†], Ji-Yu Feng[a,†], Matthias M. Minjauw[a], Eduardo Solano[b], Nithin Poonkottil[a], Michiel Van Daele[a], Ranjith K. Ramachandran[a], Chen Li[d], Sara Bals[d], Hilde Poelman[c], Christophe Detavernier[a] and Jolien Dendooven[a,*]

[a] Conformal Coating of Nanostructures (CoCooN), Department of Solid State Sciences, Ghent University, Krijgslaan 281 (S1), 9000 Ghent, Belgium

[b] NCD-SWEET beamline, ALBA Synchrotron Light Source, Carrer de la Llum 2-26, 08290 Cerdanyola del Vallès, Spain

[c] Laboratory for Chemical Technology, Ghent University, Technologiepark 125, B-9052 Zwijnaarde, Ghent, Belgium

[d] Electron microscopy for Materials research (EMAT), University Antwerpen, Groenenborgerlaan 171, B-2020 Antwerpen, Belgium

[†] these authors contributed equally

* corresponding author: jolien.dendooven@ugent.be

Abstract

Atomic layer deposition (ALD) typically employs metal precursor and co-reactant pulses to deposit thin films in a layer-by-layer fashion. While conventional ABAB-type ALD sequences implement only two functionalities, namely a metal source and ligand exchange agent, additional functionalities have emerged, including etching and reduction agents. Herein, we construct gas phase sequences – coined as ALD+ – with complexities reaching beyond classic ABAB-type ALD by freely combining multiple functionalities within irregular pulse schemes, e.g. ABCADC. The possibilities of such combinations are explored as a smart strategy to tailor bimetallic thin film and nanoparticle (NP) properties. By doing so, we demonstrate that bimetallic thin films can be tailored with target thickness and through the full compositional range, whilst the morphology can be flexibly modulated from thin films to NPs by shuffling the pulse sequence. These complex pulse schemes are expected to be broadely applicable, but are here explored for Pd-Ru bimetallic thin films and NPs.

Introduction

Atomic layer deposition (ALD) is a thin-film deposition technique that enables conformal coating of nanomaterials with (sub-)monolayer thickness control.[1–4] A classic, binary ALD process consists of cyclic exposures of a substrate to two 'components': (1) metal precursors, providing the metal source, and (2) co-reactants. These co-reactants remove the remaining ligands of the surface-anchored metal precursors and prepare the film surface for reaction in the subsequent ALD cycle. During the past decade, however, novel combinatorial ALD-based approaches have been explored which combine two binary ALD processes, yielding ternary ALD (Fig. 1).[5] While binary ALD typically produces A_xC_z compounds (e.g. Al_2O_3, ZnO, Fig. 1, left) or A metals (e.g. Pt, Pd), ternary ALD can yield $A_mB_nC_o$ compounds or A_mB_n bimetallic alloys which include two metal-types by combining two binary processes (Fig. 1, middle). A great advantage of such ternary process is its 'hierarchical' nature: supercycles can be composed beyond the binary ALD process level by depositing k x ALD cycles of process I followed by l x ALD cycles of process II (Fig. 1, right-top: k,l = 1). This flexibility of ternary ALD not only allows

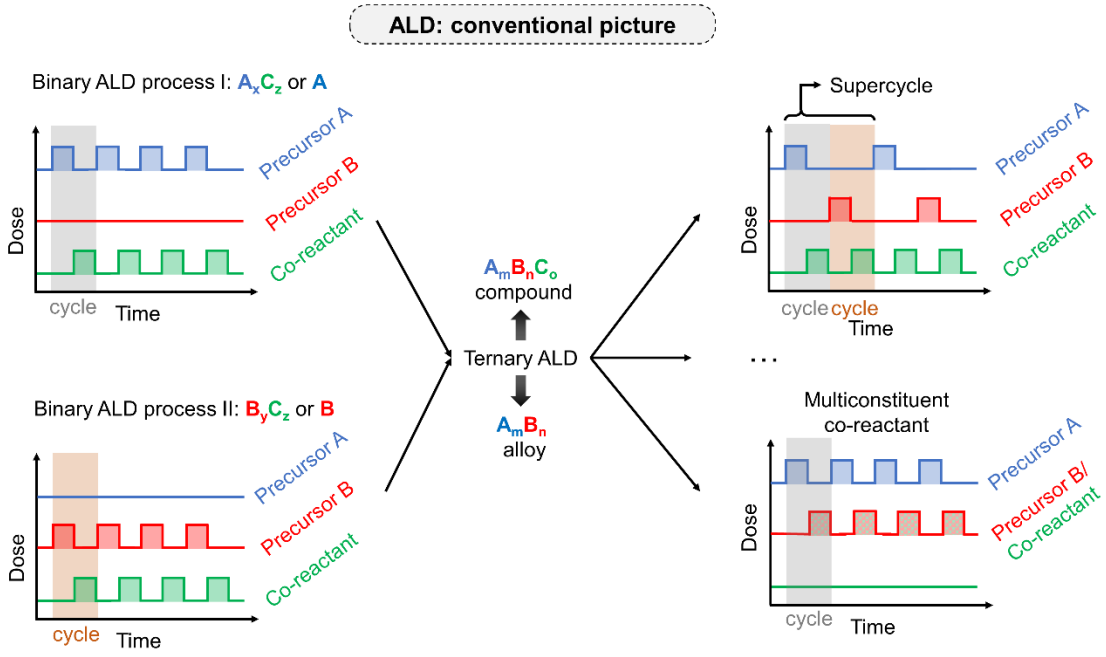

Fig. 1. Overview of the conventional picture of binary (left) and ternary (middle, right) ALD.

full compositional freedom and thickness control of the deposited film, but also permits control over the film nanostructure. In extremis, possible film structures range from lamellar sandwich-type A_xC_z–B_yC_z–A_xC_z nano-composites (or A–B–A nanolaminates) up to A_xC_z compounds with homogeneous B-metal doping (or A-B alloys).

This immense flexibility has sparked the exploration and further development of ternary ALD processes during past years.[5] A variety of ternary ALD 'strategies' have been developed which allow $A_mB_nC_o$ (A_mB_n) deposition, including (i) co-dosing of two metal precursors in one pulse, (ii) multicomponent precursors containing two metals, and (iii) multiconstituent co-reactants[6,7]. The latter is of particular interest (Fig. 1, right-bottom), since the co-reactant has a dual function: it does not only remove the ligands of precursor A, but also introduces a secondary metal source, thus simultaneously forming metal precursor B. Recently, Minjauw et al.[8] developed ternary $Al_mRu_nO_o$ and $Pt_mRu_nO_o$ oxides by combining TMA (trimethyl aluminuim) or $MeCpPtMe_3$ precursors on the one hand as metal source A, and RuO_4 on the other hand as precursor B and co-reactant. Therein, RuO_4 is not a classic metal-organic precursor, but rather a metal-oxide monomer which employs its O-ligands to combust the remaining organic ligand (fragments) of the TMA or $MeCpPtMe_3$ precursors.

While binary, ternary and potentially quaternary, quinary, etc. ALD processes have and undoubtably will keep on advancing the field in the coming decades, these processes typically implement two common 'functionalities', namely (i) metal source and (ii) ligand exchange agent. Aside from these, additional functionalities have been reported in more advanced ALD processes. First, a reduction step can be included within each ALD cycle to obtain metallic films from (noble) metal oxides, yielding an ABC-type ALD processes.[9,10] For example, Vos et al.[11] implemented cyclic H_2 exposure after the Ru precursor and O_2 co-reactant pulses to reduce RuO_x into metallic Ru. Another functionality that can be introduced is etching, as demonstrated in the same work of Vos et al. Specifically, intermittent O_2 plasma exposures were implemented in a supercycle approach during area-selective Ru deposition as a cleaning step to increase growth selectivity of Ru (e.g. *100* x [EBCHDRu / O_2 / H_2] + *1* x O_2 plasma exposure).

It is clear that (i) multiple functions can be built into a single ALD process, e.g. metal source, ligand

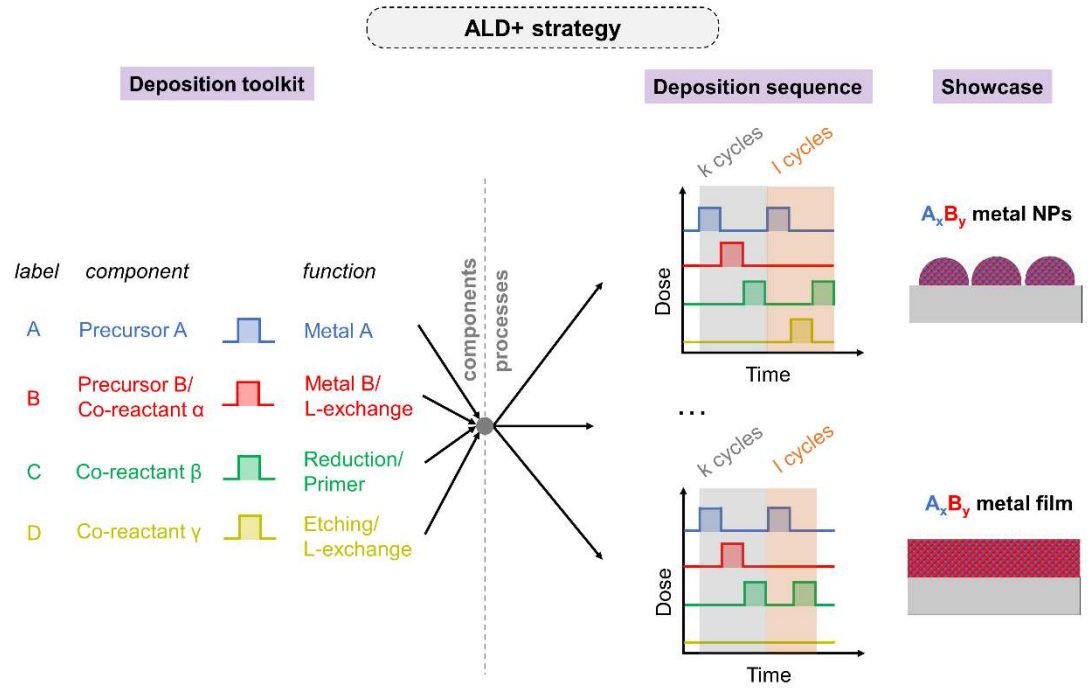

Fig. 2. Schematic overview of the ALD+ strategy demonstrated in the current work.

exchange agent, reductant and etching step (see Vos et al.[11]), but also that (ii) single pulses within the ALD process – here termed 'components' – can fullfill multiple functions, e.g. metal source as well as ligand exchange agent for multi-constituent co-reactant (see Minjauw et al.[8]). Inspired by the diversity of these functionalities and the ability of ALD to implement them flexibly, herein, we freely sequence different functionalities to construct the ALD process. Particularly, we assemble a broad toolbox of components, i.e. gas phase pulses A-D, which have different – and potentially multiple – functionalities (Fig. 2, left). By combining these components in a deliberate fashion beyond classic AB- or ABC-type ALD sequences, we exploit the possibilities of such non-classic combinations as a smart strategy to tailor the properties of bimetallic thin films and NPs (Fig. 2, right). By doing so, we demonstrate that bimetallic thin films can be obtained of which the thickness, composition and morphology can be modulated flexibly by shuffling the ALD components.

This conceptual strategy is explored for the fabrication of Pd-Ru alloyed thin films and NPs, but is more generally applicable to other systems. As ALD components here explored, Pd hexa-fluoroacetylacetonate ($Pd(hfac)_2$) and RuO_4 metal precursors are combined with H_2* and O_2* plasma as co-reactant pulses into four different processes. While $Pd(hfac)_2$ (Precursor A) has a single function as metal source, RuO_4 (Precursor B/Co-reactant α) combusts remaining organic ligands as co-reactant but simultaneously functions as a metal source. H_2* plasma (Co-reactant β) is implemented as reductant to generate bimetallic alloys but also as a primer to terminate the deposited Pd-Ru surface with H to allow Pd deposition during the subsequent Pd pulse.[12] O_2* plasma (Co-reactant γ) can combust remaining organic ligands but also functions as etching agent of Ru. The specific choices of these components originate from merging the individual components employed in the monometallic Ru (RuO_4 / H_2* plasma) and Pd ($Pd(hfac)_2$ / H_2* plasma) ALD, while O_2* is a proven etching agent for Ru demonstrated by Vos et al..

Materials and methods section

ALD was performed in a homebuilt reactor.[13] The reactor had a vacuum chamber which was connected to a turbo pump through a pneumatic gate valve. A rotation pump and bypass line were used to pump

either the chamber roughly or the backside of the turbo. With this system, a base pressure of ca. 1×10^{-6} mbar could be obtained during the ALD processes. Solid or liquid precursors ($Pd(hfac)_2$ and ToRuS™, i.e. RuO_4 dissolved in a methyl ethyl fluorinated solvent), kept in glass or stainless steel bubblers, were introduced into the chamber through stainless steel tubes, as well as the high purity gases (H_2 and O_2) used in the processes. Samples were heated to 100℃ by resistive heaters during the ALD processes. Meanwhile, the vacuum chamber was heated to 90℃, while the Pd (Ru) precursor tubes were heated to 80℃ (45℃) to avoid precursor condensation during the delivery. The Pd precursor bubbler was kept at 50℃, while ToRuS™ did not require heating. An inductively coupled radio-frequency plasma source was also installed on the chamber for surface cleaning and plasma-enhanced ALD processes.

ALD deposition was performed on Si substrates with few-nm thick native SiO_2 oxide layer. A 10s O_2* exposure on the substrate was carried out before the processes to clean surface contamination from the environment. The so-called static exposure mode was used for the $Pd(hfac)_2$ precursor pulse, meaning that the chamber was not pumped while injecting the agent. Ar (99.9999%) was used as the carrier gas for the exposure. After 10s injection of the Pd precursor, the chamber reached a pressure of ca. 1 mbar, followed by another 7s dwell time. Hence, the total exposure time was marked as 17s. The static pulse was also applied for the Ru precursor, where the exposure time was 15s, including 6s injection time and 9s dwell time. Because of the high vapor pressure of ToRuS™, no carrier gas was needed, and the static pressure could reach ca. 1.8 mbar. The exposure times of H_2* and O_2* were 10s and 5s, respectively, with a triggering power of 100W. The pressure in the chamber was 1.2×10^{-2} mbar for both plasmas.

The home-built reactor used in this work was specially designed for in situ grazing incidence small angle X-ray scattering (**GISAXS**) and X-ray fluorescence (**XRF**) measurements. The in situ experiments were performed at the SIXS beamline of the SOLEIL synchrotron. Every 2 or 5 ALD cycles, when the chamber was pumped down, an X-ray beam of 12.0 keV was focussed at the sample with an incident angle of 0.5°. The GISAXS images were recorded by an Eiger 1M 2D detector, positioned at 3.923 m from the sample, and the XRF spectra were recorded by a Vortex energy-dispersive silicon drift detector at the same time, using an acquisition time of 30s.

The film thickness was determined by X-ray reflectivity (**XRR**), while the crystal structure of the thin films was detected by X-ray diffraction (**XRD**), using a Bruker D8 system with Cu Kα radiation (λ =1.5406Å). XRF measurements were performed using a Bruker Artax XRF system with Mo X-ray source and an XFlash 5010 silicon drift detector. The Pd loading (surface density in atoms/nm^2) was determined by ex situ XRF measurements, which were calibrated with Rutherford backscattering spectrometry (**RBS**). Based on four reference ALD Pd samples (nanoparticles on SiO_2), a linear relationship was obtained between the XRF intensity of the Pd L_α lines and the RBS results. For the RBS measurement, the samples were irradiated with a 1.57 MeV He^+ beam at a tilt angle of 5°, and the backscattered ions were recorded by means of a passivated implanted planar silicon (PIPS) detector with a scattering angle of 167°. The Ru loading was determined in a similar way. Unless stated otherwise, the ratio of Ru and Pd in the bimetallic thin films or nanoparticles is determined from XRF results. **XPS** was performed on a Thermal Scientific Theta Probe XPS instrument. The surface morphology of the bimetallic thin films and nanoparticles was characterized by scanning electron microscopy (**SEM**), using an FEI Quanta 200F instrument. Ex situ grazing incidence wide-angle X-ray scattering (**GIWAXS**) measurements were performed at the NCD-SWEET beamline of the ALBA synchrotron light source (Spain). A monochromatic X-ray beam of 12.4 keV (λ=0.9998Å) was set by a Si (111) channel cut monochromator and the incident angle was 0.1° to ensure the surface sensitivity. A Rayonix LX255-HS area detector was used to record the 2D scattering patters. The exiting angles were calibrated using Cr_2O_3 as calibration

standard, which resulted in a sample-detector distance of 0.142 m. Recorded GIWAXS data was reduced to 1D azimuthal profiles by using a python routine based on pyFAI.[14] Two Thermo Fisher Scientific probe-corrected Titan microscopes were operated at 300 kV in the mode of scanning transmission electron microscopy (**STEM**) for taking high-angle annular dark-field (**HAADF**) images. A probe current of 50 pA was used for HAADF imaging, and 150 pA was used for Electron energy loss spectroscopy (**EELS**) spectrum imaging.

Results and Discussion

Step I: depositing bimetallic thin films in a 3-pulse ALD process

A first step in increasing ALD complexity is to combine Pd and Ru metal sources in a single process to deposit bimetallic thin films and compare to their monometallic analogues. **Fig. 3a** schematically shows the process sequences of the (top) monometallic Pd [$Pd(hfac)_2$ / H_2*], (middle) monometallic Ru [RuO_4 / H_2*] and (bottow) bimetallic Pd-Ru ALD processes [$Pd(hfac)_2$ / RuO_4 / H_2*]. In the latter process, RuO_4 presents as a multiconstituant co-reactant, since it fullfills a dual function as co-reactant to combust the hfac-ligands after $Pd(hfac)_2$ exposure but also as Ru source.[8] The final H_2* plasma pulse of the bimetallic process also fullfills two functions: (i) reduction of the oxidized surface to obtain bimetallic instead of oxide films, (ii) H-termination of the thin film surface as a 'primer' for subsequent Pd deposition,[12] thus allowing continuous Pd-on-Ru growth. The gas phase components used to deposit the Pd-Ru bimetallic film at 100°C on a SiO_2/Si substrate are presented in **Fig. 3b**. **Fig. 3c** shows the film thickness against the number of ALD cycles, obtained for the two reference processes for monometallic growth of Ru (red circles) and Pd (blue triangles) and the three-step Pd-Ru process (black squares). The Ru-containing processes, i.e. [$Pd(hfac)_2$ / RuO_4 / H_2*] and [RuO_4 / H_2*], exhibit a direct linear growth behavior without any nucleation delay, in stark contrast to the [$Pd(hfac)_2$ / H_2*] process, for which almost no growth (0.4 nm) is achieved even after 100 cycles. The long nucleation delay during Pd ALD is in agreement with previous studies,[15] and is mainly due to the formation of inactive dissociated species on the oxide support upon $Pd(hfac)_2$ exposure, blocking the nucleation sites for Pd growth.[16] The great enhancement of the nucleation achieved when RuO_4 is added in between $Pd(hfac)_2$ and H_2* indicates that RuO_4 reacts with the organic ligand (fragments) of $Pd(hfac)_2$. In addition, no nucleation delay is observed for the [RuO_4 / H_2*] process, causing the substrate oxide surface to be readily covered with a monolayer of Ru-Pd metal after the [$Pd(hfac)_2$ / RuO_4 / H_2*] cycle, where substrate surface poisoning with the hfac ligands is further avoided and rapid growth can be established. The growth per cycle (GPC) is extracted by fitting a linear curve to the sets of data points using a least-squares method. Similar high GPCs are acquired for the RuO_4 containing processes, namely 0.19 ± 0.01 nm/cycle for both Ru-Pd and pure Ru. The steady state growth rate of [$Pd(hfac)_2$ / H_2*] amounts to 0.021 nm/cycle, being ~10 times lower compared to RuO_4-containing processes. Our previous work shows a nucleation delay of around 20 cycles and a lower GPC of ca. 0.14 nm/cycle[17] when performing the [RuO_4 / H_2*]. For the latter process, however, a low RuO_4 exposure pressure of 9×10^{-3} mbar was used, while in this work a static pulse at 1.8 mbar is applied.

The thicknesses of the ALD grown thin films were determined by XRR measurements. **Fig. 3d** shows the XRR spectra (black curves) and the corresponding simulations (red curves) obtained for as-deposited films grown by performing the [$Pd(hfac)_2$ / RuO_4 / H_2*] process for 10, 20, 50 and 100 cycles. The reflectivity patterns contain different numbers of periodic intensity oscillations of varying amplitudes, reflecting different thicknesses of the films. The close agreement of the experimental and simulated spectra highlights the formation of continuous thin films even with 10 ALD cycles. The simulated result including thickness (T), roughness (R), and density (D) for each sample is shown in the left-bottom part

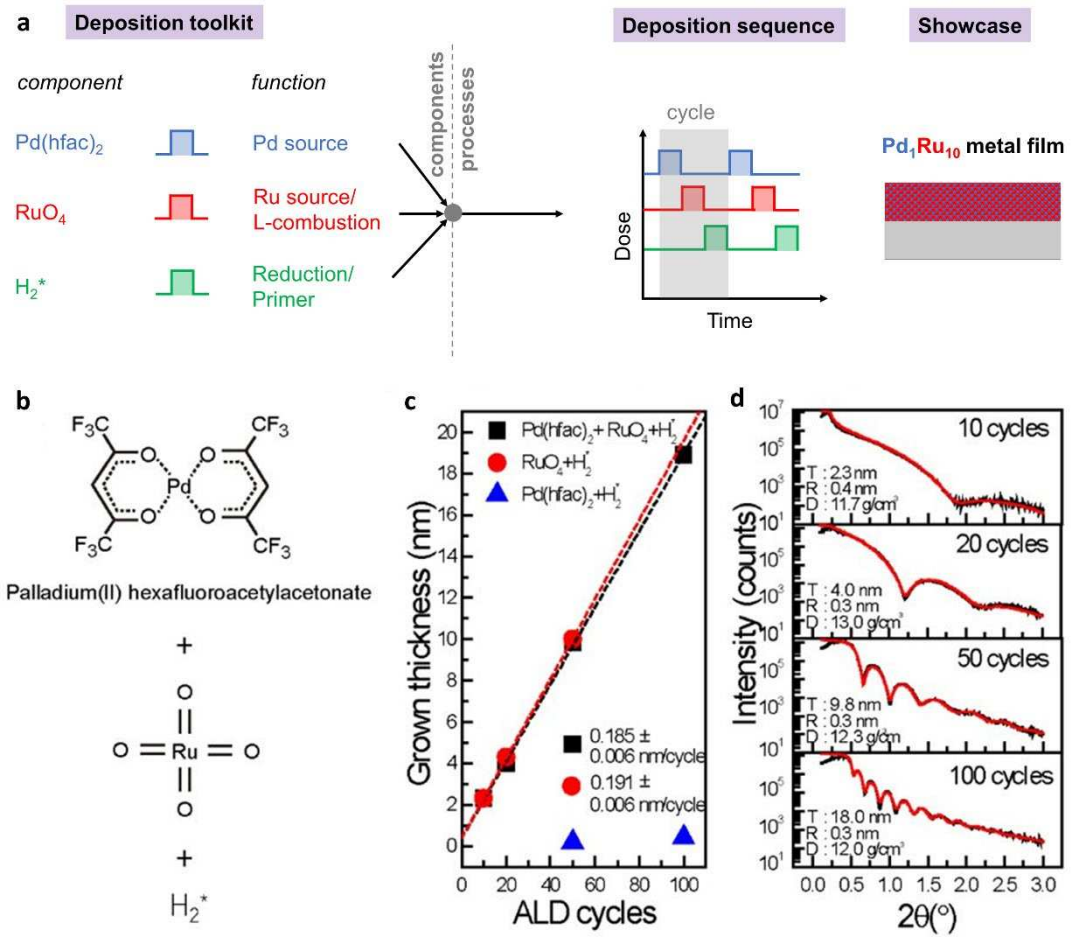

Fig. 3. a) Schematic representation of the [$Pd(hfac)_2$ / RuO_4 / H_2*] process components, deposition sequence and thin film deposition. b) Chemical structure of the ALD sequence components of the [$Pd(hfac)_2$ / RuO_4 / H_2*] process. c) Grown thicknesses as a function of ALD cycles obtained by the three-step process and two reference processes ([RuO_4 / H_2*] and [$Pd(hfac)_2$ / H_2*]). d) The experimental (black curves) and simulated (red curves) XRR spectra measured from as-deposited thin films obtained by performing the three-step process for 10, 20, 50, and 100 cycles. The simulated results including thickness (T), roughness (R), and density (D) are shown in the left-bottom part.

of the corresponding graphs. The low roughness remains stable (~0.3 nm) when the thickness increases, as well as the density of the thin films, diplaying a value of ca. 12 g/cm^3, in line with the densities of pure bulk Pd (12.023 g/cm^3) and Ru (12.45 g/cm^3).

The saturation behaviour of the [$Pd(hfac)_2$ / RuO_4 / H_2*] process was tested by performing 50 cycles of this process on SiO_2/Si substrates at 100°C with variations in the pulsing time of each agent (**Fig. 4**). The grown thicknesses (vertical axis) and the corresponding GPCs (horizontal axis) remain unchanged when increasing the $Pd(hfac)_2$ and RuO_4 exposure time (**Fig. 4a** and **4b**). For the H_2* pulse, saturation is achieved for pulsing times of 10s and more, while a substantially higher GPC is found when 5s H_2* is used. The XRR result reveals that the density of the films deposited by the process with 5s H_2* is only 7.75 g/cm^3, suggesting that the H_2* exposure is not sufficient to fully reduce the thin film surface after RuO_4 exposure, indicating that O impurities are incorporated in the as-deposited film. This phenomenon was also observed in the previously reported [RuO_4 / H_2*] process.[17]

As a test experiment, an ALD process comprising only the two metal sources is tested, i.e. [$Pd(hfac)_2$ /

RuO_4] and compared to the three component [$Pd(hfac)_2$ / RuO_4 / H_2*] process. Only in the latter case, growth is observed. This phenomenon is different from the Al- and Pt-ruthenates ($Al_xRu_yO_z$ or $Pt_xRu_yO_z$) grown in Minjauw et al.[8], where [TMA / RuO_4] and [$MeCpPtMe_3$ / RuO_4] ALD processes yield Al- or Pt-ruthenates without reducing agents. This shows that $Pd(hfac)_2$ requires a fully reduced metal surface with H terminal groups to allow for reaction, and thus deposition.

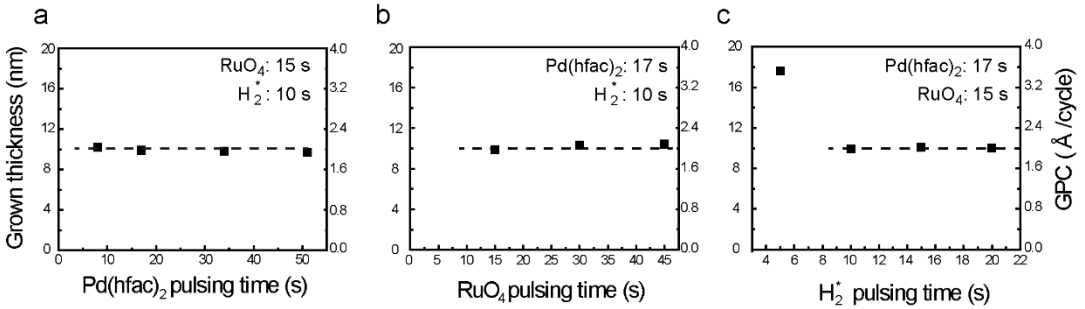

Fig. 4. a) The grown thicknesses (left axis) and the corresponding GPC (right axis) obtained by the [$Pd(hfac)_2$ / RuO_4 / H_2*] process with variations in a) $Pd(hfac)_2$ pulsing time, b) RuO_4 pulsing time and c) H_2* pulsing time. Every ALD thin film was deposited by applying 50 cycles of the three-step process on a SiO/Si substrate at 100°C.

The composition of the as-deposited thin film is determined by XPS and XRF. **Fig. 5a** and **5b** show the recorded Pd 3d and Ru 3p spectra. The presence of the Pd $3d^{5/2}$ and $3d^{3/2}$ and the Ru $3p^{3/2}$ and $3p^{1/2}$ double peaks reveals that Pd and Ru atoms are indeed present in the as-deposited films. The XPS-obtained atomic ratio of Pd to Ru is 1:9, meaning that the ALD-deposited film is a Pd-doped Ru thin film. XPS also indicates that fluorine (F) and oxygen (O) signals are under the detection limit, suggesting that the hfac-ligands are removed. Due to the overlap in the peak positions of C 1s and Ru 3d peaks, the deconvolution of the XPS spectra is not reliable to determince the carbon contribution independently. **Fig. 5c** shows the XRF spectrum covering the range of the Pd L and Ru L lines. The convoluted Pd L and Ru L signals can be distinguished through simulation and the atomic ratio of Pd to Ru determined by XRF is 1:10, which is in close agreement with the XPS result. Interestingly, the atomic ratios of Pd:Ru of ~1:10 are in line with the ~10 times higher growth rates for RuO_4-containing processes compared to the [$Pd(hfac)_2$ / H_2*] process.

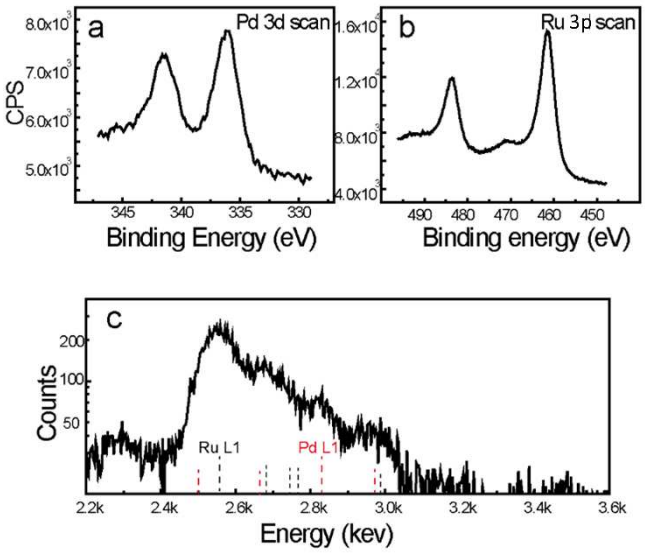

Fig. 5. XPS spectra of a) Pd 3d and b) Ru 3p scans; c) XRF spectrum for the 18.9 nm Ru-Pd bimetallic thin film deposited by 100 cycles of the [$Pd(hfac)_2$ / RuO_4 / H_2*] process on a SiO_2/Si substrate.

The crystalline nature of the ALD-deposited film is characterized by XRD (**Fig. 6**). The diffractogram of the Pd-Ru thin film after 100 x [$Pd(hfac)_2$ / RuO_4 / H_2*] cycles on SiO_2/Si (yielding an XRR-thickness of 18.9 nm) shows a polycrystalline Ru hcp structure with several crystal orientations, i.e. Ru(100), Ru(002) and Ru(101) (JCPDS 65-1863). No diffractions corresponding to Pd fcc are present. This indeed confirms that the Pd atoms are doped in the Ru grains of the polycrystalline film without forming phase-separated fcc Pd crystals. The diffraction peak located at ~33.0° is the Si(002) peak from the substrate.[18]

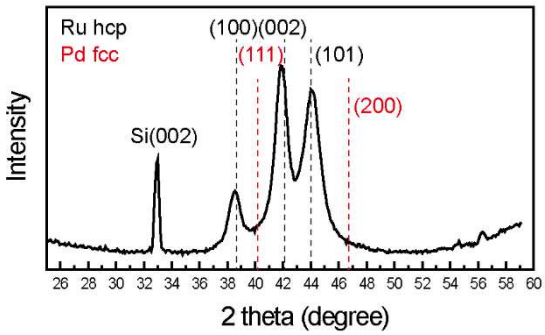

Fig. 6. XRD diffractogram for the 18.9 nm Pd-Ru thin film deposited by performing 100 x [$Pd(hfac)_2$ / RuO_4 / H_2*] cycles on a SiO_2/Si at 100°C. The expected peak diffraction of Ru hcp and Pd fcc are indicated by black and red dashed lines, respectively. The diffraction peak locating at ~33.0° corresponds to the Si(002) plane from the substrate.

In summary, the [$Pd(hfac)_2$ / RuO_4 / H_2*] ALD sequence only requires three gas-phase pulses per ALD cycle to deposit bimetallic thin film. This reduces the deposition time and gas consumption during the ALD process compared to the more conventional 4-step [$Pd(hfac)_2$ / H_2* / RuO_4 / H_2*] sequence, consisting of serial [$Pd(hfac)_2$ / H_2*] and [RuO_4 / H_2*] monometallic processes. Notably, the nucleation delay observed for [$Pd(hfac)_2$ / H_2*] on SiO_2/Si surfaces is not manifested when RuO_4 is added as intermediate pulse, directly yielding uniform thin films with low roughness. However, the compositional tunability of the thin film from the 3-step process is limited, resulting in bimetallic films with fixed atomic stoichiometry (Pd_1Ru_{10} from XRF). In the following, compositional flexibility in the Pd-Ru thin film is introduced by increasing the process complexity, initiating from the [$Pd(hfac)_2$ / RuO_4 / H_2*] ALD 3-step sequence.

Step II: tuning the bimetallic thin film thickness and composition

To control the composition of the Pd-Ru thin films, the relative number of RuO_4 to $Pd(hfac)_2$ exposures should be reduced. Therefore, a supercycle protocol is implemented which contains k x [$Pd(hfac)_2$ / RuO_4 / H_2*] + (20 – k) x [$Pd(hfac)_2$ / H_2*] cycles. Each supercycle thus contains 20 individual ALD cycles, either [$Pd(hfac)_2$ / RuO_4 / H_2*] or RuO_4-free [$Pd(hfac)_2$ / H_2*], in total leading to 20 $Pd(hfac)_2$ pulses and a variable number k of RuO_4 exposures (k = 0, 1, 2, 4, 10, 20) (**Fig. 7a**).

Fig. 7b shows the XRR-derived thicknesses of the bimetallic thin films as a function of the total number of ALD cycles, corresponding to the number of $Pd(hfac)_2$ exposures in the ALD sequence. **Fig. 7b** reveals that the growth rate decreases with a reducing number k of RuO_4 exposures included in the process. The GPC is ~0.19nm/cycle if each ALD cycle within the supercycle includes a RuO_4 exposure (k = 20), while

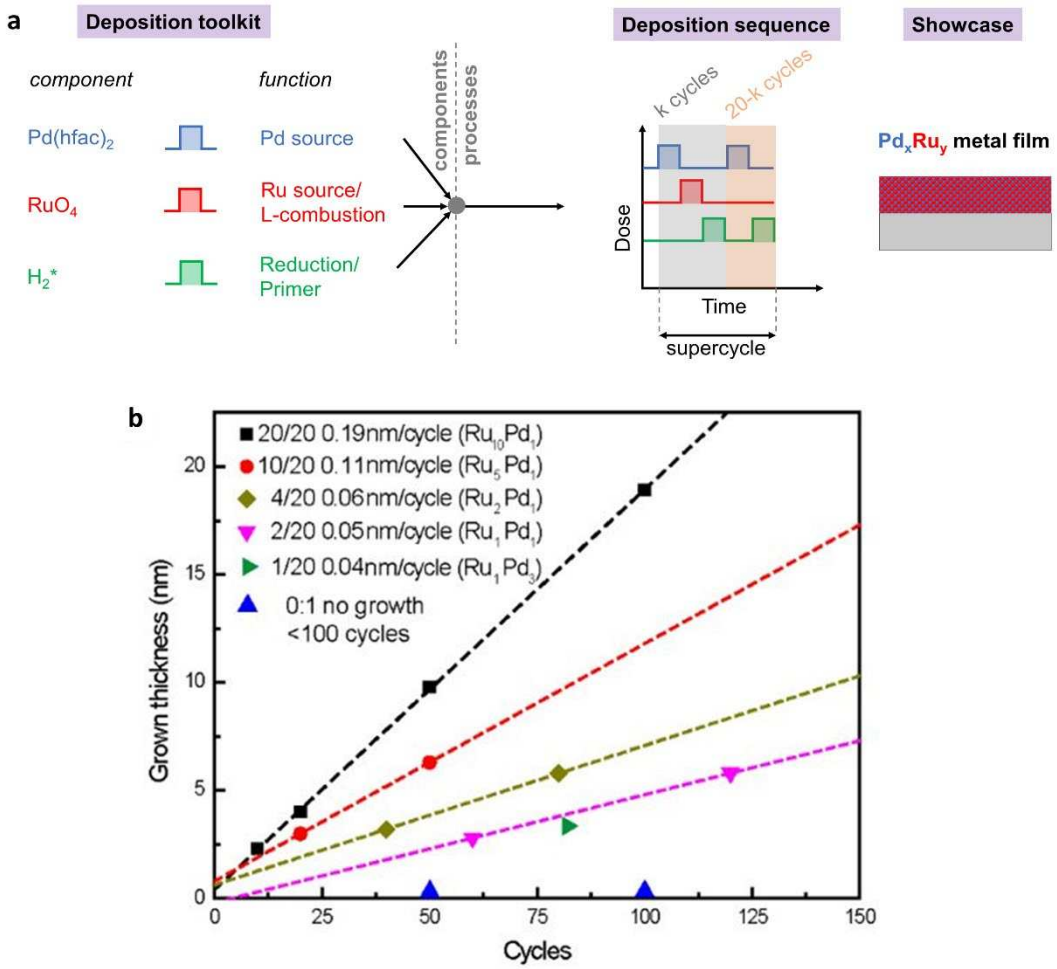

Fig. 7. a) Scheme of the *k* x [Pd(hfac)$_2$ / RuO$_4$ / H$_2$*] + (20 – *k*) x [Pd(hfac)$_2$ / H$_2$*] ALD supercycle approach to deposit Pd$_x$Ru$_y$ thin films. b) ALD grown thickness vs the number of ALD cycles, corresponding to the number of Pd(hfac)$_2$ exposures of the sample. In the legend, *k*/20 is indicated, which presents the number of *k* cycles are selected within the supercycle, in total consisting of 20 individual ALD cycles.

it decreases to ~0.04nm/cycle when only one RuO$_4$ exposure is implemented (*k* = 1). With less RuO$_4$ exposures in the supercycle sequence, the Pd concentration increases as expected. Because of its high growth rate, only a single RuO$_4$ exposure in each supercycle (*k* = 1) results in a 1:3 atomic ratio of Ru:Pd. When decreasing the number of RuO$_4$ exposures *k* from 20 to 1 in the supercycle, the Ru concentration in the bimetallic thin film declines from ca. 91% to 25%, obtained via XRF-RBS (Experimental section). The linear curves in **Fig. 7b** indicate that a low *k*-value within the supercycle results in drastically enhanced nucleation and prevents growth inhibition, compared to the monometallic [Pd(hfac)$_2$ / H$_2$*] process (*k* = 0) where no significant growth is observed below 100 ALD cycles. The surface morphology of as-deposited Pd-Ru bimetallic thin films with similar thicknesses (~2-3 nm) is characterized by SEM, as shown in **Fig. 8**. The [Pd(hfac)$_2$ / RuO$_4$ / H$_2$*] process (*k* = 20) results in a 2.3 nm continuous Pd-doped Ru film on SiO$_2$/Si after only 10 x [Pd(hfac)$_2$ / RuO$_4$ / H$_2$*] ALD cycles, further supporting the thin film pattern observed in XRR (**Fig. 3c**). In contrast, it is well-know that [Pd(hfac)$_2$ / H$_2$*] ALD (*k* = 0) results in small dispersed nanoparticles.[19] The addition of RuO$_4$ exposures – i.e. *k* increase within the supercycle – between the Pd(hfac)$_2$ and H$_2$* can thus effectively stimulate the nucleation. Even for *k* =

1, four supercycles result in a bimetallic Pd-Ru film with 3.3 nm thickness and full surface coverage.
In summary, Pd-Ru bimetallic thin films with tunable thickness and composition can be deposited using a *k* x [$Pd(hfac)_2$ / RuO_4 / H_2*] + (20 – *k*) x [$Pd(hfac)_2$ / H_2*] supercycle approach. The thickness of the thin films can be modified by varying the number of supercycles performed during deposition, while the Ru:Pd ratio can be tuned by adjusting the *k*-value of the supercycle, i.e. by modulating the number of RuO_4 exposures in the ALD sequence. According to the variation of the GPCs at different *k*-values, one RuO_4 pulse contributes ~0.16-0.18 nm thickness per exposure, while one $Pd(hfac)_2$ pulse contributes ~0.02-0.03 nm per exposure to the bimetallic thin film (assuming Pd and Ru have similar bulk densities).

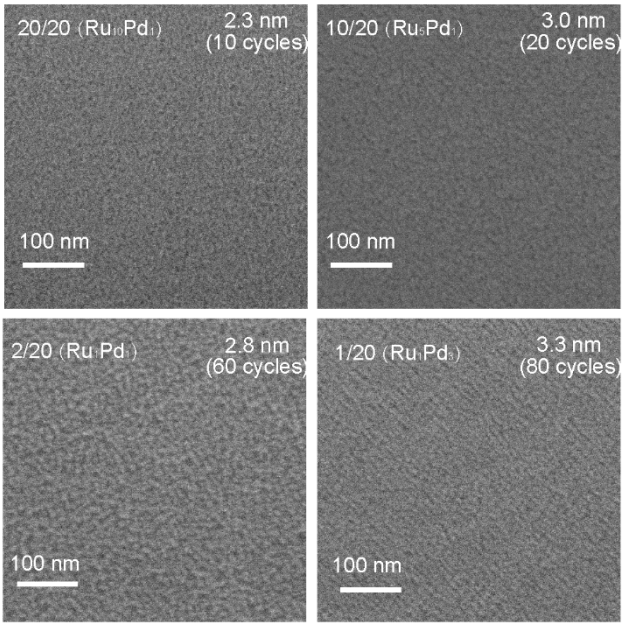

Fig. 8. Top-view SEM graphs of the bimetallic Ru-Pd thin films on SiO_2/Si deposited by *k* x [$Pd(hfac)_2$ / RuO_4 / H_2*] + (20 – *k*) x [$Pd(hfac)_2$ / H_2*] cycles with *k* = 20, 10, 2 and 1 (denoted as *k*/20 (panel-tof left), film thickness in nm (panel-tof right), # of supercycles (panel-tof right)).

Step III: transforming the morphology from bimetallic thin films to nanoparticles

Here, we show that by introducing O_2* exposures in the ALD sequence, Pd-Ru bimetallic thin films can be transformed into bimetallic nanoparticles (BMNPs). The intention behind this strategy is that O_2* plasma can selectively etch Ru (Ru(s) + O_2*(g) = RuO_4 (g)); a process leading to film break-up and restructuring into NPs. Vos et al. recently reported the selective ALD growth of Ru on Pt rather than on

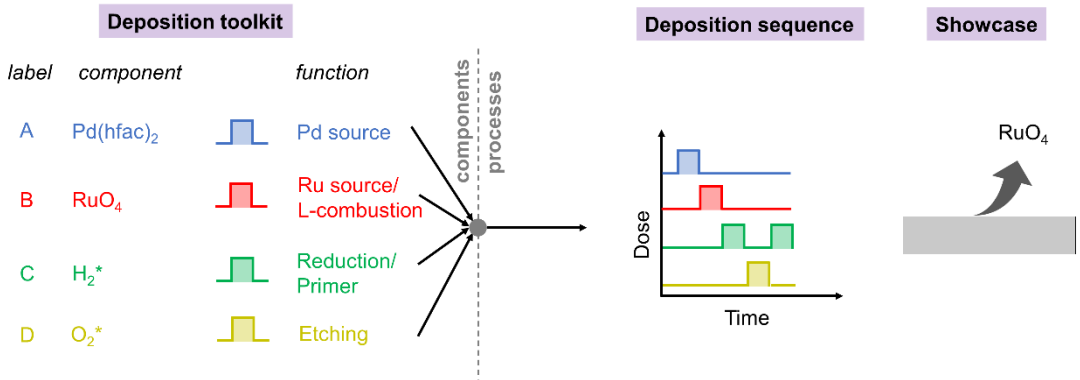

Fig. 9. Scheme of the [$Pd(hfac)_2$ / RuO_4 / H_2* / O_2* / H_2*] ALD process.

SiO_2, using intermittant O_2* plasma etch steps within the ALD process to periodically remove Ru nuclei formed on SiO_2.[11] One 30s O_2* exposure was found to effectively remove ~1 nm of Ru thin film.

As shown in **Fig. 9**, the [$Pd(hfac)_2$ / RuO_4 / H_2*] 3-pulse process, extended by an additional [O_2* (5s) / H_2* (10s)] sequence into a 5-pulse ALD cycle, is implemented to verify the etching effect of O_2*. The H_2* pulse after the O_2* etching step is used to (i) reduce the sample surface towards the metallic states, eventually obtaining bimetallics and not oxides, and (ii) as a primer to terminate the bimetallic surface with H to allow reaction with $Pd(hfac)_2$ in the subsequent pulse. This [$Pd(hfac)_2$ / RuO_4 / H_2* / O_2* / H_2*] process however shows no film growth after 10 and 20 cycles, while 20 cycles of the [$Pd(hfac)_2$ / RuO_4 / H_2*] process yields a 4 nm bimetallic thin film. It can thus be confirmed that O_2* is a strong etching agent. Since it is known that Ru is etched away, likely, the Pd-dopants dispersed in the thin film are also removed (**Fig. 10**).

In our previous work[12], a monometallic Pd ALD process comprising [$Pd(hfac)_2$ / O_2* / H_2*] sequences was reported with a relatively large GPC of ~0.04 nm/cycle at 100°C.[12] The O_2* step following the $Pd(hfac)_2$ precursor pulse can effectively combust the remaining ligands and oxidises the Pd surface, while the H_2* step reduces the Pd surface and leaves H atoms on a carbon-free surface for efficient interaction with the subsequent $Pd(hfac)_2$ precursor. Inspired by this process, the [$Pd(hfac)_2$ / RuO_4 / H_2*] 3-step process can be alternated with the just-mentioned Pd ALD process in supercycle approach, i.e. *k* x [$Pd(hfac)_2$ / RuO_4 / H_2*] + *l* x [$Pd(hfac)_2$ / O_2* / H_2*] (**Fig. 11a**). By doing so, the O_2* pulse not only functions as ligand combustion agent after the $Pd(hfac)_2$ exposure, but also etches Ru from the deposited thin film. Including the [$Pd(hfac)_2$ / O_2* / H_2*] process in the supercycle sequence yields two beneficial functionalities: (i) additional $Pd(hfac)_2$ exposures, independent of the number of RuO_4 sequences, to enrich the Pd content of the deposited bimetallics, and (ii) the O_2* etching pulse are implemented to

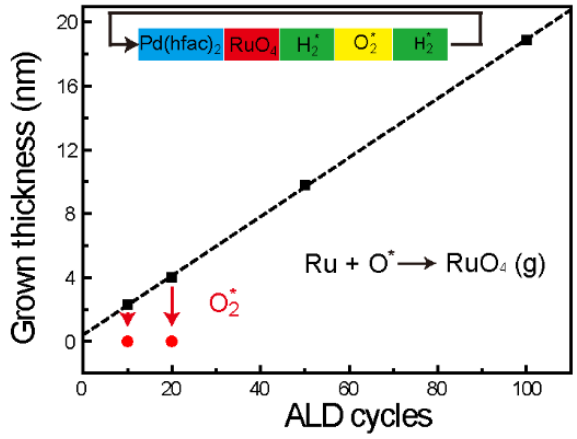

Fig. 10. O_2* etching effect on as-deposited Ru rich bimetallic thin films thickness. The dashed black line corresponds to the [$Pd(hfac)_2$ / RuO_4 / H_2*] process, while the red dots corresponds to [$Pd(hfac)_2$ / RuO_4 / H_2* / O_2* / H_2*].

reduce the Ru content and restructure the thin film into BMNPs (*vide infra*). Specifically, during the O_2* plasma pulse in the [$Pd(hfac)_2$ / O_2* / H_2*] cycle, significant quantities of Ru are etched away. This is expected to lead to thin film break-up in conjunction with restructuring into nanoparticles, in order to minimize the free energy of the system. By varying the *k*:*l* ratio within the ALD supercycle, the frequency of both processes can be controlled, allowing to modulate the Ru:Pd thin film composition and morphology (**Fig. 11b**). On the top left of each SEM sub-panel the *k*:*l* supercycle ratio is shown, yielding a specific Ru_xPd_y composition after deposition, as shown on the top right. The latter composition is extracted via the Pd and Ru counts detected in XRF. These counts are linked respectively to a specific #

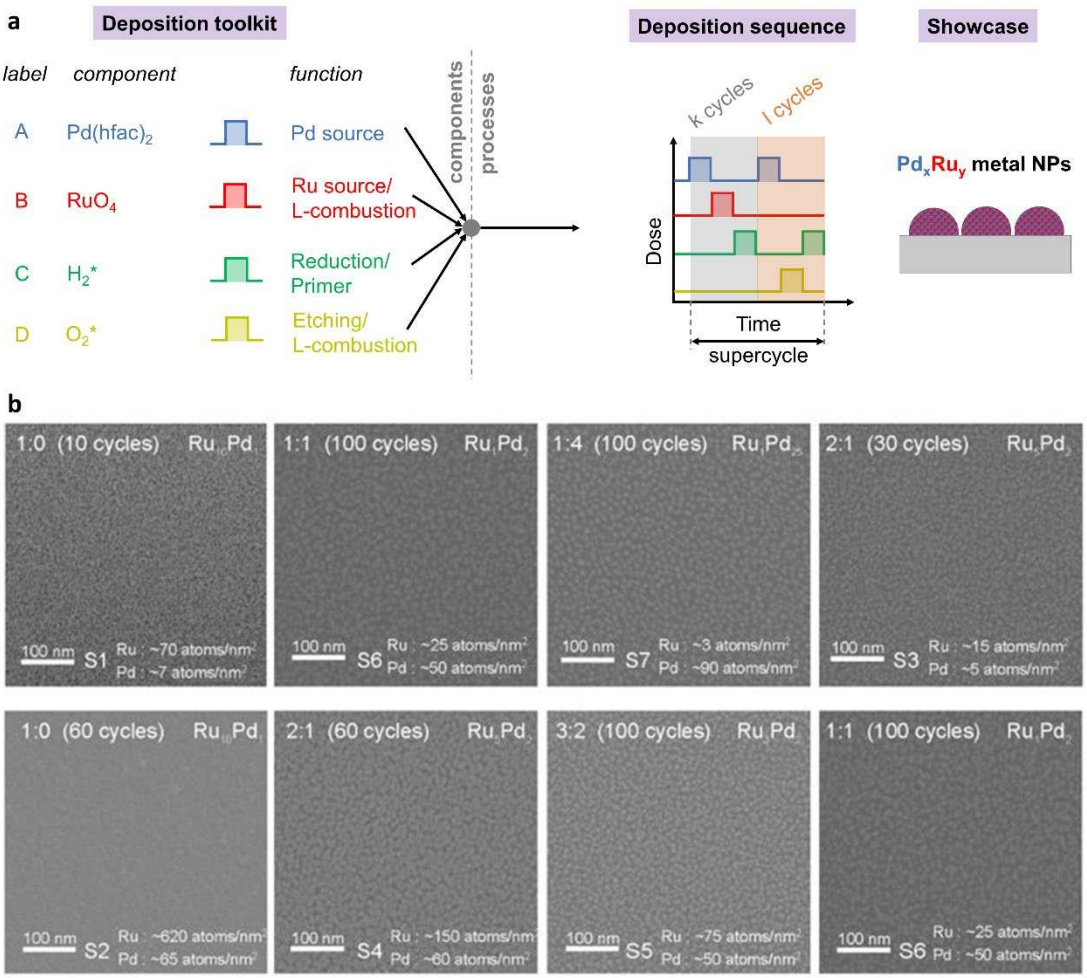

Fig. 11. a) Scheme of the *k* x [$Pd(hfac)_2$ / RuO_4 / H_2*] + *l* x [$Pd(hfac)_2$ / O_2* / H_2*] ALD supercycle sequence, yielding bimetallic Pd_xRu_y nanoparticles. b) Top-view SEM images of the ALD-deposited bimetallic nanoparticles using the scheme in a) for different *k*:*l* ratios marked, labeled as S1-S7 as a link to Table 1.

of Pd and Ru atoms/nm^2 on the SiO_2/Si substrate via RBS, shown on the bottom right of the sub-panels. The Ru_xPd_y composition can then be calculated for each *k*:*l* combination based on the # atoms/nm^2.

Table 1 shows detailed complementary information to **Fig. 11** for samples S1-S7: the process conditions, the surface metal loadings and Ru:Pd atomic ratios of the deposited materials. Note that samples S1 and S2 are grown with the three-step process discussed in 'Step I', i.e. without the use of O_2*-containing sequences, which can be considered as reference samples for the discussion below. With increasing *l* x [$Pd(hfac)_2$ / O_2* / H_2*] sequences within the supercycle the Pd content increases. This results from the increasing number of exposures of the sample to (i) the Pd source $Pd(hfac)_2$ which adds Pd and (ii) the O_2* etching agent which removes Ru. For *k*:*l* = 1:4, a highly Pd-rich Ru_1Pd_{25} alloy is obtained for *k* x [$Pd(hfac)_2$ / RuO_4 / H_2*] + *l* x [$Pd(hfac)_2$ / O_2* / H_2*] ALD supercycle sequences (**Table 1**, S7). In contrast, for *k* = 1 within the *k* x [$Pd(hfac)_2$ / RuO_4 / H_2*] + (20 – *k*) x [$Pd(hfac)_2$ / H_2*] ALD supercycle sequence, only Ru_1Pd_3 alloys are obtained with 75% of Pd (**Fig. 7b**). This is due to the etching effect of O_2* which removes Ru from the film. Moreover, when comparing S1 and S6, it is found that bimetals with a total loading of ~75 atoms/nm^2 can be deposited after only 10 ALD cycles without O_2*-containing sequences, while 100 cycles are needed to achieve this loading when half of the cycles contain O_2* ([$Pd(hfac)_2$ / O_2* / H_2*]). Nevertheless, both S6 and S7 are deposited by 100 cycles of the ALD processes

with a different *k*:*l* ratio, but share a similar total loading (~75 and ~93 atoms/nm^2). This shows that the [Pd(hfac)$_2$ / O$_2$* / H$_2$*] process not only etches Ru but also deposits Pd, which can compensate for the Ru loss. In addition, S1/S2 and S3/S4 further indicate that the metal loading of the as-deposited material increases with the total number of ALD cycles, and the Pd and Ru composition remains unchanged. However, the growth is not linear with the number of ALD cycles.

Table 1. Detailed information on Ru-Pd bimetallic nanoparticles (S1-S7) deposited by the *k* x [Pd(hfac)$_2$ / RuO$_4$ / H$_2$*] + *l* x [Pd(hfac)$_2$ / O$_2$* / H$_2$*] process, including the ratio of the [Pd(hfac)$_2$ / RuO$_4$ / H$_2$*] to [Pd(hfac)$_2$ / O$_2$* / H$_2$*] cycles (*k*:*l*), total # ALD cycles, XRF-derived Ru, Pd and total metal loadings/nm^2 and the Ru/Pd atomic ratio expressed as Ru$_x$Pd$_y$ for each sample.

No.	*k*:*l*	cycles	Pd loading (atoms/nm^2)	Ru loading (atoms/nm^2)	Total loading (atoms/nm^2)	Denoted as (Ru/Pd atomic ratio)
S1	1:0	10	~7	~70	~77	Ru$_{10}$ Pd$_1$
S2	1:0	60	~65	~620	~685	Ru$_{10}$ Pd$_1$
S3	2:1	30	~5	~15	~20	Ru$_5$ Pd$_2$
S4	2:1	60	~60	~150	~210	Ru$_5$ Pd$_2$
S5	3:2	100	~50	~75	~125	Ru$_3$ Pd$_2$
S6	1:1	100	~50	~25	~75	Ru$_1$ Pd$_2$
S7	1:4	100	~90	~3	~93	Ru$_1$ Pd$_{25}$

Top-view SEM images in **Fig. 11b** show the surface morphology of S1-S7. The three images on the left of the 1st row correspond to S1, S6 and S7 and have similar metal loading (**Table 1**). The images reveal that bimetallic Pd-Ru NPs rather than thin films are formed when [Pd(hfac)$_2$ / O$_2$* / H$_2$*] cycles are included in the supercycle sequence (S6-7, $l > 0$), in contrast to the homogenous film structure of S1 ($l = 0$). Comparing the SEM images in **Fig. 8** and **Fig. 11b** further illustrates that the *k* x [Pd(hfac)$_2$ / RuO$_4$ / H$_2$*] + (20 – *k*) x [Pd(hfac)$_2$ / H$_2$*] strategy enables Ru-Pd thin film deposition, while the *k* x [Pd(hfac)$_2$ / RuO$_4$ / H$_2$*] + *l* x [Pd(hfac)$_2$ / O$_2$* / H$_2$*] strategy allows the formation of nanoparticles. SEM images from S3 and S4 clearly show an increase of the particle size, coalescence and total loading of the BMNPs when increasing the number of total cycles. S2 and S4-6 on the second row in **Fig. 11b** have similar Pd (50~60 atoms/nm^2) but varying Ru loading (~620, ~150, ~75 and ~25 atoms/nm^2), S2 being a reference grown without O$_2$* containing [Pd(hfac)$_2$ / O$_2$* / H$_2$*] cycles. The SEM images of S4-S6 indicate that the NP size increases with increasing Ru loading, but that there is no significant difference in their areal density.

To further probe the evolution of the Ru-Pd BMNP morphology during ALD, synchrotron-based in situ GISAXS-XRF is conducted (SIXS-SOLEIL, France). **Fig. 12** shows the GISAXS patterns of Ru-Pd BMNPs with a total loading of ~50, ~100, and ~200 atoms/nm^2, as determined by in situ XRF, recorded during three different *k* x [Pd(hfac)$_2$ / RuO$_4$ / H$_2$*] + *l* x [Pd(hfac)$_2$ / O$_2$* / H$_2$*] ALD processes: (1) *k*:*l* = 1:0 (S1), (2) *k*:*l* = 3:2 (S5), (3) *k*:*l* = 1:4 (S7). The GISAXS patterns obtained for the [Pd(hfac)$_2$ / RuO$_4$ / H$_2$*] three-step process (*k*:*l* = 1:0 (S1)) exhibit no clear off-axis ($Q_y \neq 0$ nm^{-1}) scattering features on the 2D screen. This suggests that a flat thin film is formed from the early stage of the process onward. In comparison, clear scattering features are observed in the GISAXS patterns for the other three O$_2$*-containing processes (S5, S7), revealing the presence of non-randomly distributed NPs with a statistical average center-to-center distance. Morphological information such as the average width, height and

interparticle distance of the nanoparticles are included in the GISAXS pattern, through the Q_y and Q_z positions of the minima (white arrows-size) and the Q_y positions of the maxima (white dashed lines-distance). **Fig. 12** reveals that the average center-to-center distance, width and height of the BMNPs increase with increasing total loading from ~50 to ~200 atoms/nm^2, in opposite to the decreasing trend of the corresponding indicators, since it is in the reciprocal space. This is in line with the expected growth and coalescence of the BMNPs. The BMNP widths W and heights H are derived via 'fast analysis'[12] using the correlations: $W = 8.8/q_{y,min}$ and $H = 2\pi/\Delta q_{z,min}$. W and H range between 5.8–8.8 nm and 4.2–6.3 nm, respectively, for showcases where $l \neq 0$. Interestingly, the BMNPs with different Ru/Pd atomic ratio (and *k*:*l* ratio) but same loading display a similar GISAXS pattern – and thus NP morphology. This result shows that the total loading has impact on the size and spacing (due to coalescence) of the BMNPs, while the Ru/Pd atomic ratio only does to a lesser extent. This visually confirms the suggestions observed via SEM.

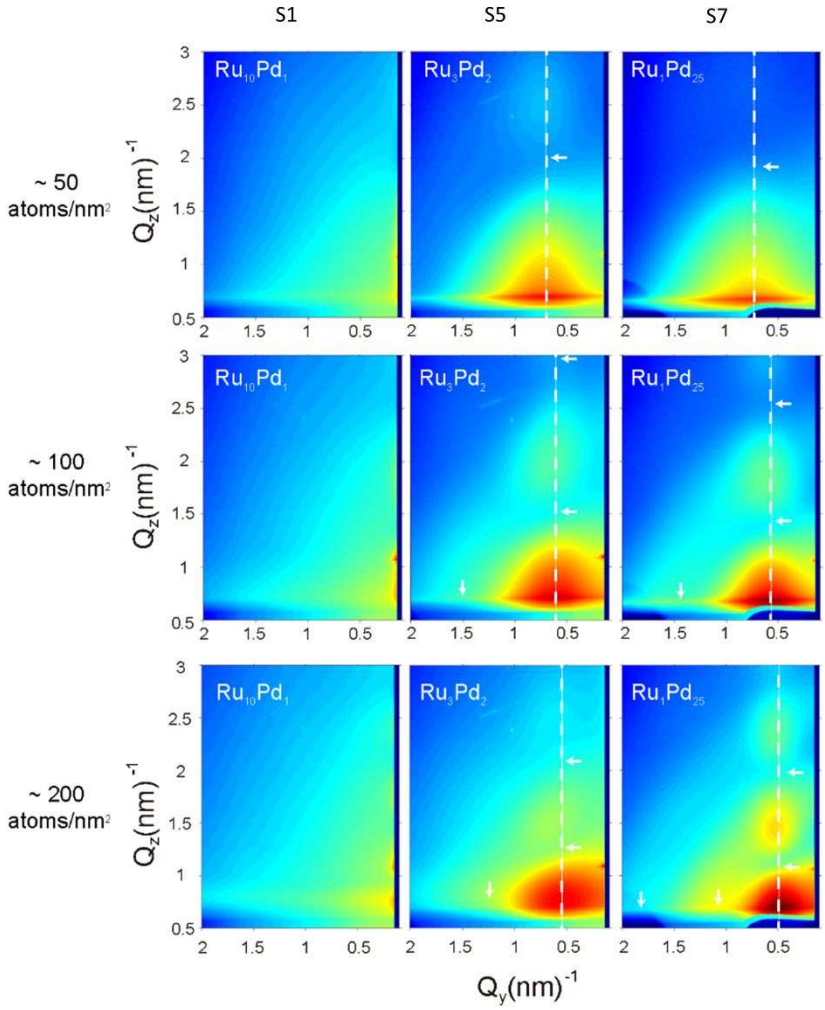

Fig. 12. In situ GISAXS patterns of BMNPs at ~50, ~100, and ~200 atoms/nm^2 deposited by *k* x [Pd(hfac)$_2$ / RuO$_4$ / H$_2$*] + *l* x [Pd(hfac)$_2$ / O$_2$* / H$_2$*] ALD processes: (1) *k*:*l* = 1:0 (S1), (2) *k*:*l* = 3:2 (S5), (3) *k*:*l* = 1:4 (S7).

The crystal structures of the obtained BMNPs are investigated by synchrotron-based GIWAXS (λ = 0.9998Å, SWEET-NCD, ALBA, Spain). **Fig. 13a** shows the ex situ 1D-integrated diffractograms of the BMNPs with different compositions, i.e. $Ru_{10}Pd_1$ (S1), Ru_5Pd_2 (S4), Ru_3Pd_2 (S5), Ru_1Pd_2 (S6) and

Ru_1Pd_{25} (S7) with 2θ ranging from 20°-60°. Ru-rich $Ru_{10}Pd_1$ (S1) and Pd-rich Ru_1Pd_{25} (S7) NPs on SiO_2/Si display the diffraction patterns corresponding to hcp Ru and fcc Pd, resp. (JCPDS 65-1863, 65-2867). In contrast, Ru_5Pd_2 (S4) and Ru_3Pd_2 (S5) nanoparticles have a diffraction pattern comprising both hcp and fcc structures, where the peak positions are shifted relative to reference monometallic Ru and Pd positions. This suggests the co-existence of both Ru hcp and Pd fcc crystal structures for S4 and S5. With increasing Pd concentration, the dominant diffractions of the Ru-Pd BMNPs gradually changes from hcp to fcc. **Fig. 13b** displays the diffractograms with 2θ ranging from 20°-35°, which gives a more detailed evolution from Ru hcp ((100), (002) and (101)) to Pd fcc ((111) and (200)) with increasing Pd content in the BMNPs. Note that the Ru hcp Bragg peak positions of S1 are shifted to lower 2θ angles compared to the pattern in Fig. 6 as a result of a higher X-ray energy used to record the XRD pattern.

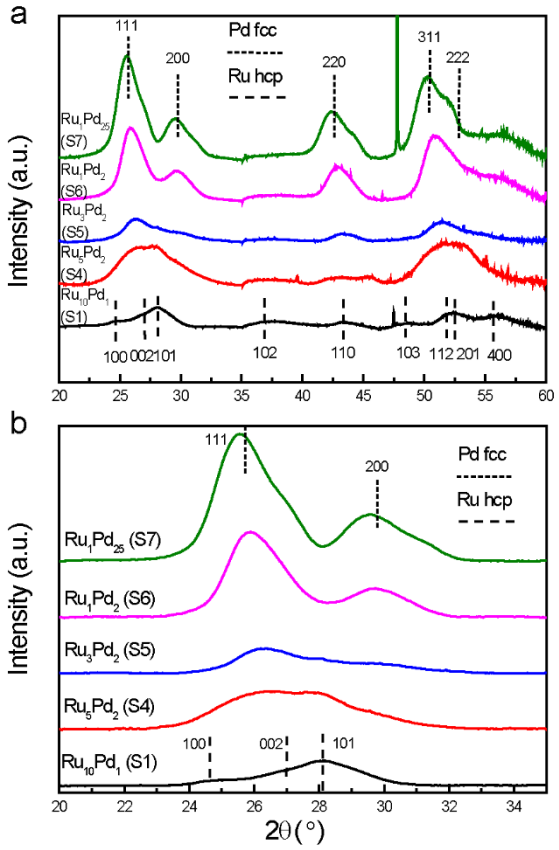

Fig. 13. GIWAXS diffractograms (λ = 0.9998 Å) for the Ru-Pd BMNPs with different Ru/Pd atomic ratios (S1, S4-S7) deposited by the *k* x [$Pd(hfac)_2$ / RuO_4 / H_2*] + *l* x [$Pd(hfac)_2$ / O_2* / H_2*] ALD process: *k*:*l* = 1:0 (S1), *k*:*l* = 2:1 (S4), *k*:*l* = 3:2 (S5), *k*:*l* = 1:1 (S6), *k*:*l* = 1:4 (S7), a) with 2θ from 20° to 60° and b) from 20° to 35°. The reference Ru hcp and Pd fcc diffraction peak positions are indicated by long and short dashed lines, respectively.

To probe the mixing intimacy of Pd and Ru within the BMNPs, STEM is used (**Fig. 14**). Ru-Pd BMNPs for STEM are deposited by performing 30 supercycles of the 2 x [$Pd(hfac)_2$ / RuO_4 / H_2*] + 1 x [$Pd(hfac)_2$ / O_2* / H_2*] process on a silicon nitride (Si_3N_4) mesh substrate (same as S4). The HAADF-STEM image shows nanoparticles (brighter areas) with 2~3 nm in size on a support (**Fig. 14a).** Since Pd and Ru have a similar atomic number (46 and 44), the strong difference in intensity of the nanoparticles and the thin

film should originate from metals and the Si_3N_4 substrate, rather than the segregation of either Ru or Pd. EELS is carried out on a selected nanoparticle projection area (**Fig. 14b**). The EELS elemental mappings of Ru and Pd (**Fig. 14c, Fig. 14d**) show that the two metals are homogeneously distributed across the NP. This result provides visual evidence of the atomic-level intimate mixing of the Ru-Pd alloys.

It should be noted that Ru and Pd are not immiscible at the atomic level in the bulk state according to the phase diagram.[20] However, it was recently reported that the synthesis of Ru-Pd solid-solution (alloy nanoparticles) over the whole composition range could be achieved through chemical reduction methods[21] and atomic diffusion strategy.[22] It seems that the physical and chemical properties are quite different from the bulk state when the size of Ru-Pd bimetallic system decreases to the nanoscale, for which further investigation is still needed.[23] The proposed method in this work for precise size- and composition-controlled synthesis of Ru-Pd nanoalloys provides the possibility for a systematic study.

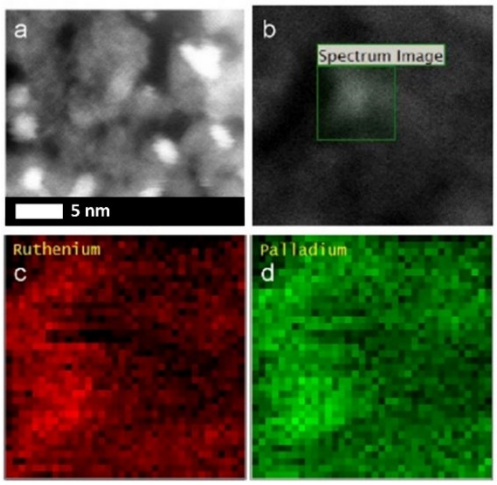

Fig. 14. a) and b) HAADF-STEM images obtained for the Ru-Pd BMNPs on the Si_3N_4 mesh substrate, deposited by 30 supercycles of the 2 x [$Pd(hfac)_2$ / RuO_4 / H_2*] + 1 x [$Pd(hfac)_2$ / O_2* / H_2*] process (the same as S4). EELS elemental mappings of c) Ru and d) Pd in the selected area of a nanoparticle in b).

Conclusions

Herein, we constructed gas phase sequences with complexities beyond classic ABAB-type ALD by freely combining multiple functionalities within irregular pulse schemes, e.g. ABCADC. The possibilities of such non-classic combinations are explored as a smart strategy to tailor bimetallic thin film and nanoparticle (NP) properties, here showcased on Pd-Ru. As a first step, the [$Pd(hfac)_2$ / RuO_4 / H_2*] ALD sequence allows bimetallic Pd-Ru thin film deposition with reduced deposition time and gas consumption compared to more conventional 4-step [$Pd(hfac)_2$ / H_2* / RuO_4 / H_2*]. The nucleation delay observed for Pd deposition during monometallic [$Pd(hfac)_2$ / H_2*] ALD disappears when combined with RuO_4 in the three-step process, this boosting Pd deposition. Further increasing deposition complexity, by pulsing k x [$Pd(hfac)_2$ / RuO_4 / H_2*] + (20 – k) x [$Pd(hfac)_2$ / H_2*] supercycles allows to modulate the Pd-Ru film composition across the full compositional range. Specifically, high (low) k values lead to Pd poor (rich) films, while the number of executed supercycles controls the film thickness. Aside from composition and thickness control, the morphology of the deposited materials could be controlled via k x [$Pd(hfac)_2$ / RuO_4 / H_2*] + l x [$Pd(hfac)_2$ / O_2* / H_2*] ALD supercycles, where l x [$Pd(hfac)_2$ / O_2* / H_2*] cycles are included (i) to increase the Pd content and (ii) O_2* plasma pulses as etching steps. These complex pulse schemes are expected to be broadly applicable, but are here explored for Pd-Ru bimetallic thin films and NPs.

Acknowledgements

This research was funded by the Research Foundation – Flanders (FWO) and the Special Research Fund BOF of Ghent University (GOA 01G01019). M. F. and M. M. M. acknowledge the FWO for a postdoctoral research fellowship (1280621N). N. P. acknowledges the European Union's Horizon 2020 research and innovation program under the Marie Skłodowska-Curie grant agreement no. 765378. For the GISAXS measurements, the authors received funding from the European Community's Trans-national Access Program CALIPSOplus. E.S. acknowledges the Spanish project RTI2018-093996-B-C32 MICINN/FEDER funds. Air Liquide is acknowledged for supporting this research. We acknowledge SOLEIL for provision of synchrotron radiation facilities and we would like to thank Dr. Alessandro Coati for assistance in using beamline SiXS. The GIWAXS experiments were performed at NCD-SWEET beamline at ALBA Synchrotron with the collaboration of ALBA staff.

References

(1) Leskelä, M.; Ritala, M. Atomic Layer Deposition Chemistry: Recent Developments and Future Challenges. *Angew. Chem. Int. Ed.* **2003**, *42* (45), 5548–5554.

(2) George, S. M. Atomic Layer Deposition: An Overview. *Chem. Rev.* **2010**, *110* (1), 111–131.

(3) Puurunen, R. L. Surface Chemistry of Atomic Layer Deposition: A Case Study for the Trimethylaluminum/Water Process. *J. Appl. Phys.* **2005**, *97* (12), 121301.

(4) Oviroh, P. O.; Akbarzadeh, R.; Pan, D.; Coetzee, R. A. M.; Jen, T.-C. New Development of Atomic Layer Deposition: Processes, Methods and Applications. *Sci. Technol. Adv. Mater.* **2019**, *20* (1), 465–496.

(5) Mackus, A. J. M.; Schneider, J. R.; MacIsaac, C.; Baker, J. G.; Bent, S. F. Synthesis of Doped, Ternary, and Quaternary Materials by Atomic Layer Deposition: A Review. *Chem. Mater.* **2019**, *31* (4), 1142–1183.

(6) Gebhard, M.; Letourneau, S.; Mandia, D. J.; Choudhury, D.; Yanguas-Gil, A.; Mane, A.; Sattelberger, A. P.; Elam, J. W. Formation of Unsaturated Hydrocarbons and Hydrogen: Surface Chemistry of Methyltrioxorhenium(VII) in ALD of Mixed-Metal Oxide Structures Comprising Re(III) Units. *Chem. Mater.* **2019**, *31* (19), 7821–7832.

(7) Ritala, M.; Kukli, K.; Rahtu, A.; Räisänen, P. I.; Leskelä, M.; Sajavaara, T.; Keinonen, J. Atomic Layer Deposition of Oxide Thin Films with Metal Alkoxides as Oxygen Sources. *Science* **2000**, *288* (5464), 319–321.

(8) Minjauw, M. M.; Feng, J.-Y.; Sajavaara, T.; Detavernier, C.; Dendooven, J. Atomic Layer Deposition of Ternary Ruthenates by Combining Metalorganic Precursors with RuO_4 as the Co-Reactant. *Dalton Trans.* **2021** (DOI: 10.1039/D1DT03543F)

(9) Hämäläinen, J.; Ritala, M.; Leskelä, M. Atomic Layer Deposition of Noble Metals and Their Oxides. *Chem. Mater.* **2014**, *26* (1), 786–801.

(10) Lu, J.; Low, K.-B.; Lei, Y.; Libera, J. A.; Nicholls, A.; Stair, P. C.; Elam, J. W. Toward Atomically-Precise Synthesis of Supported Bimetallic Nanoparticles Using Atomic Layer Deposition. *Nat. Commun.* **2014**, *5*, 3264.

(11) Vos, M. F. J.; Chopra, S. N.; Verheijen, M. A.; Ekerdt, J. G.; Agarwal, S.; Kessels, W. M. M.; Mackus, A. J. M. Area-Selective Deposition of Ruthenium by Combining Atomic Layer Deposition and Selective Etching. *Chem. Mater.* **2019**, *31* (11), 3878–3882.

(12) Feng, J.-Y.; Minjauw, M. M.; Ramachandran, R. K.; Daele, M. V.; Poelman, H.; Sajavaara, T.; Dendooven, J.; Detavernier, C. The Co-Reactant Role during Plasma Enhanced Atomic Layer

Deposition of Palladium. *Phys. Chem. Chem. Phys.* **2020**, *22* (16), 9124–9136.

(13) Dendooven, J.; Solano, E.; Minjauw, M. M.; Van de Kerckhove, K.; Coati, A.; Fonda, E.; Portale, G.; Garreau, Y.; Detavernier, C. Mobile Setup for Synchrotron Based in Situ Characterization during Thermal and Plasma-Enhanced Atomic Layer Deposition. *Rev. Sci. Instr.* **2016**, *87* (11), 113905.

(14) Kieffer, J.; Valls, V.; Blanc, N.; Hennig, C. New Tools for Calibrating Diffraction Setups. *J. Synchr. Rad.* **2020**, *27* (2), 558–566.

(15) Ten Eyck, G. A.; Senkevich, J. J.; Tang, F.; Liu, D.; Pimanpang, S.; Karaback, T.; Wang, G.-C.; Lu, T.-M.; Jezewski, C.; Lanford, W. A. Plasma-Assisted Atomic Layer Deposition of Palladium. *Chem. Vap. Dep.* **2005**, *11* (1), 60–66.

(16) Goldstein, D. N.; George, S. M. Surface Poisoning in the Nucleation and Growth of Palladium Atomic Layer Deposition with $Pd(Hfac)_2$ and Formalin. *Thin Solid Films* **2011**, *519* (16), 5339–5347.

(17) Minjauw, M. M.; Dendooven, J.; Capon, B.; Schaekers, M.; Detavernier, C. Atomic Layer Deposition of Ruthenium at 100 °C Using the RuO_4-Precursor and H_2. *J. Mater. Chem. C* **2014**, *3* (1), 132–137.

(18) Zaumseil, P. High-Resolution Characterization of the Forbidden Si(200) and Si(222) Reflections. *J. Appl. Cryst.* **2015**, *48* (2), 528–532.

(19) Feng, J.-Y.; Ramachandran, R. K.; Solano, E.; Minjauw, M. M.; Van Daele, M.; Vantomme, A.; Hermida-Merino, D.; Coati, A.; Poelman, H.; Detavernier, C.; Dendooven, J. Tuning Size and Coverage of Pd Nanoparticles Using Atomic Layer Deposition. *App. Surf. Sci.* **2021**, *539*, 148238.

(20) Tripathi, S. N.; Bharadwaj, S. R.; Dharwadkar, S. R. The Pd-Ru System (Palladium-Ruthenium). *J. Phase Equil.* **1993**, *14* (5), 638–642.

(21) Kusada, K.; Kobayashi, H.; Ikeda, R.; Kubota, Y.; Takata, M.; Toh, S.; Yamamoto, T.; Matsumura, S.; Sumi, N.; Sato, K.; Nagaoka, K.; Kitagawa, H. Solid Solution Alloy Nanoparticles of Immiscible Pd and Ru Elements Neighboring on Rh: Changeover of the Thermodynamic Behavior for Hydrogen Storage and Enhanced CO-Oxidizing Ability. *J. Am. Chem. Soc.* **2014**, *136* (5), 1864–1871.

(22) Wu, D.; Cao, M.; Shen, M.; Cao, R. Sub-5 Nm Pd–Ru Nanoparticle Alloys as Efficient Catalysts for Formic Acid Electrooxidation. *ChemCatChem* **2014**, *6* (6), 1731–1736.

(23) Wu, D.; Kusada, K.; Kitagawa, H. Recent Progress in the Structure Control of Pd–Ru Bimetallic Nanomaterials. *Sci. Technol. Adv. Mater.* **2016**, *17* (1), 583–596.

Table of Contents Graphic